

# Realisation of ground state and thermally inaccessible configurations in artificial kagome dipolar spin ice

Jack C. Gartside<sup>1\*</sup>, Daan M. Arroo<sup>1</sup>, David M. Burn<sup>2</sup>, Victoria L. Bemmer<sup>3</sup>, Andy Moskalenko<sup>1</sup>,  
Lesley F. Cohen<sup>1</sup> and  
Will R. Branford<sup>1</sup>

Blackett Laboratory, Imperial College London<sup>1</sup>  
Diamond Light Source, Didcot<sup>2</sup>  
Department of Materials, Imperial College London<sup>3</sup>

September 12, 2017

## Abstract

Arrays of non-interacting nanomagnets are widespread in data storage and processing. As current technologies approach fundamental limits on size and thermal stability, enhancing functionality through embracing the strong interactions present at high array densities becomes attractive. In this respect, artificial spin ices are geometrically-frustrated magnetic metamaterials offering vast untapped potential from their unique microstate landscapes, with intriguing opportunities from reconfigurable logic to magnonic devices or hardware neural networks. However, progress in such systems is impeded by the inability to access more than a fraction of the total microstate space. Here, we demonstrate that topological defect-driven magnetic writing - a scanning probe technique - provides access to all possible microstates in artificial spin ices and related arrays of nanomagnets. In particular, we create previously elusive configurations such as the spin-crystal ground state of artificial kagome dipolar spin ice and high-energy, low-entropy ‘monopole-chain’ states exhibiting negative effective temperatures.

Artificial spin ices (ASI) are magnetic metamaterials comprised of strongly-interacting nanomagnets, each acting as a single ‘macrospin’, in geometrically frustrated arrays. The macrospins obey magnetic equivalents of Pauling’s ice-rules<sup>1</sup>, arranging themselves to minimise net magnetic charge  $q_m$  at each vertex. ASI<sup>2</sup> has provided vital physical insight on diverse topics from magnetic monopole-like excitations<sup>3,4</sup> to fundamental thermodynamics<sup>5-10</sup>. Key to its promise is the enormous number of unique magnetic charge configurations (or microstates) and the possibility to directly image the magnetic structure. A kagome (honeycomb) ASI array containing  $N$  vertices possesses  $\sim \frac{3}{\sqrt{2}}^N$  microstates satisfying the ice-rules, yielding vast microstate landscapes. The ice-rule obeying states all possess near-equivalent energies leading to massive degeneracy, inviting deep thermodynamic studies<sup>10</sup>

---

\*j.carter-gartside13@imperial.ac.uk

as well as device-focused applications exploiting the microstate landscape to store information<sup>11,12</sup> or function as a hardware neural-network<sup>5,9,13</sup> or reconfigurable magnonic crystal<sup>14,15</sup>. However, the full potential of ASI is unrealised as conventional state-preparation techniques access only a tiny fraction of the total microstate space. Consider a six-macrospin hexagon of kagome ASI, possessing  $2^6 = 64$  metastable magnetic configurations (local minima in the potential energy surface). Typically a globally uniform external magnetic field initialises state  $A$  and then drives magnetic reversal to state  $B$ . As each bar switches only once, six additional states are sampled and so 57 states are never accessed. Energy barriers between states vary largely so few low-energy pathways from  $A$  to  $B$  exist. Most states do not lie on any of these pathways, rendering them inaccessible via global magnetic field protocols. In a typical  $10^3$  macrospin array just  $10^{-296}\%$  of possible states are sampled in a global-field driven magnetic reversal. Thermal activation and subsequent annealing of ASI can randomly sample low-energy microstates inaccessible using external global fields<sup>10,16-19</sup>. However, the exact final state cannot be specified and to-date it has not been possible to explore the network of microstates sufficiently to prepare a system in the dipolar kagome ASI ground state<sup>18</sup>. The limited state-writing functionality has impeded progress in ASI, therefore developing a protocol for the precise control of individual macrospins is crucial to revealing the entire ASI manifold and the rich physics within.

Scanning-probe techniques offer an ever-broadening suite of tools for exquisite nanoscale patterning<sup>20</sup>, including topographical modification<sup>21,22</sup>, molecular synthesis<sup>23</sup> and recently nanomagnetic writing. Localised modification of magnetic anisotropy in thin-films via a heated tip and global H field<sup>24</sup>, scanning tunneling microscope switching of superparamagnetic islands in cryogenic conditions<sup>25</sup>, magnetic-force microscope (MFM) tip-mediated domain wall (DW) injection<sup>26</sup> and a combined MFM-tip and global-field protocol for selective remagnetisation of weakly-interacting nanowires<sup>27</sup> represent key advances in the field, forging paths for new work in fundamental and device physics. Here, we present ‘topological defect-driven magnetic writing’ (TMW) - a novel, powerful magnetic patterning technique for directly injecting topological defects<sup>28</sup> in magnetic nanowires. These defects propagate through structures as DWs, achieving controlled and reversible writing of magnetisation states in the process with no external global fields required. Working in ambient conditions, TMW reveals the entire microstate landscape of ASI and related nanopatterned magnetic systems. We demonstrate several previously unobserved states including ‘monopole chains’, high-energy low-entropy ASI configurations inaccessible by conventional means and exhibiting negative effective temperatures<sup>29</sup>, and the spin-crystal ground state of kagome ASI<sup>16,18,30</sup>.

## Working principle of topological defect-driven magnetic writing

TMW is depicted schematically in fig. 1 a) with a corresponding micromagnetic time evolution series shown in fig. 1 b). We first demonstrate TMW experimentally in a simple system of parallel 1-4.8  $\mu\text{m}$  NiFe nanowires. Figure 1 c) shows an MFM image of nanowires after initialisation in a global field  $H_{sat}$ . Figure 1 d) shows the same nanowires after selective magnetic reversal, with blue arrows denoting switched wires.

TMW consists of passing a commercially available high-moment MFM tip over a nanostructure at a tip-sample separation of  $r \approx 5 - 10$  nm, with the tip moving perpendicular to the long-axis of the structure. At these small tip-sample separations, the tip field  $H_{tip}$  may be treated using a point-probe approximation<sup>31,32</sup> as having a monopole-like form  $H_{tip} = \frac{\mu_0}{4\pi r^2} q_{tip}$  where  $q_{tip}$  is the magnetic charge of the tip. The nanowire begins the process

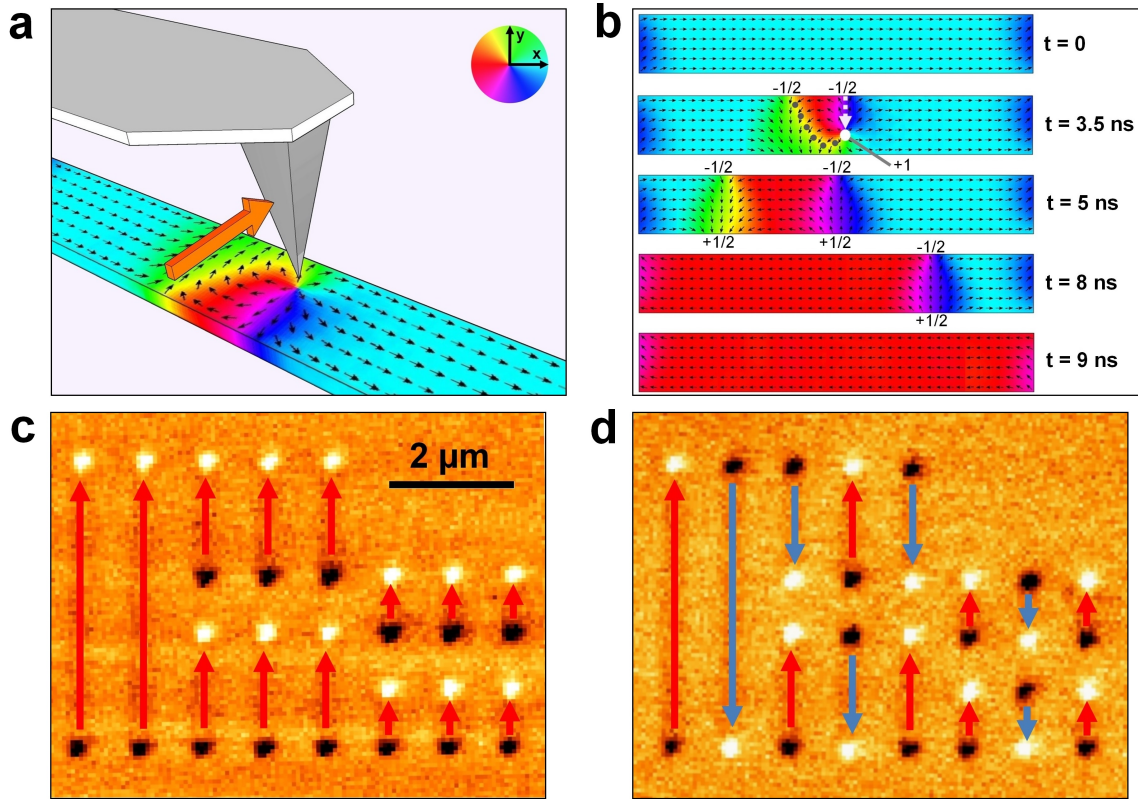


**Figure 1: The topological defect-driven magnetic writing process.** a) Schematic of TMW operation. An MFM-tip induced vortex is moved through a nanostructure spin texture by the motion of the tip. Colour wheel represents magnetisation direction in panels a) and b), orange arrow denotes  $v_{tip}$ .

b) Micromagnetic simulation of the time-evolution of the TMW write-function used to reverse the magnetisation of a  $500 \times 75 \times 10$  nm nanowire. The MFM tip and its direction of motion are represented by the white circle and dashed arrow respectively. Topological defects are labelled with their winding numbers. A video of this process is available in the supplementary materials.

c, d) MFM images of  $10 \times 100$  nm<sup>2</sup> cross-section NiFe nanowires of 1, 2 and 4.8  $\mu$ m length, (c) after initialisation with global field and (d) after TMW-switching of selected wires. Light and dark contrast indicate positive and negative magnetic charge respectively. Overlaid arrows show magnetisation direction as a guide to the eye, red arrows indicate unwritten wires, blue arrows show TMW-written wires.

in a single-domain ferromagnetic state ( $t = 0$  in fig. 1 b). The tip then approaches the structure and at sufficient values of  $H_{tip}$  the spins in the wire rearrange themselves to lie along the radial tip field, lowering their Zeeman energy. Around the apex of the tip ( $t = 3.5$  ns, represented by the white circle) these realigned spins form a vortex configuration due to the locally divergent shape of  $H_{tip}$ <sup>33,34</sup>. The vortex remains directly under the tip as the tip crosses the wire, forming a pair of  $180^\circ$  DWs in its wake in the process. An in-depth discussion of how the direct manipulation of topological defects drives DW formation is provided in the supplementary information, and is similar to the  $360^\circ$  DW injection process previously described<sup>26</sup>.

The DW formation process is asymmetric between the left and right-hand DWs: On one side (right of tip in fig. 1 b) the component of  $H_{tip}$  along the wire-length is parallel to the wire magnetisation, so any disturbance to the micromagnetic structure is minimal. On the other side  $H_{tip}$  is anti-parallel to the magnetisation and drives local magnetic reversal. This forces the left-hand DW into a curved, elongated shape around the nascent left-magnetised domain created between the DWs, shown by the grey dotted line fig. 1 b),  $t = 3.5$  ns.

The distorted shape of the left-hand DW has an associated micromagnetic energy penalty relative to the straight, shorter right-hand DW. Once the tip crosses the wire the left-hand DW straightens out, assuming a lower energy conformation and gaining momentum in the process. The DW accelerates left towards the end of the wire, aided by a magnetostatic attraction between the DW magnetic charge and the magnetic charge of the wire-end. On reaching the left-end of the structure, the DW is free to unwind into a collinear spin state ( $t = 8$  ns), lowering the system energy. The remaining right-hand DW also experiences a magnetostatic attraction to the structure ends. Providing the tip crosses the structure slightly to the right of centre, the net force on the remaining DW is directed to the right. This pulls the DW into the right-hand end of the structure where it also unwinds on contact, leaving the wire DW-free with a magnetisation anti-parallel to its initial state. The TMW writing process is now complete.

Whether the right or left-hand DW forms in a high-energy state is decided by a combination of the nanostructure's initial magnetisation and the magnetisation of the MFM tip, allowing the user to tailor the writing dynamics simply by remagnetising the tip. The combination depicted in fig. 1 b) arises from a right-magnetised nanostructure and MFM tip magnetised into the page. Reversing either magnetisation will result instead in the right-hand DW forming in a high-energy state and accelerating once the tip passes. Reversing both has no effect. Simulated videos of the writing process for various magnetisation combinations are provided in the supplementary materials. It is worth noting that  $H_{tip}$  is insufficient to switch wires by proximity alone; if the tip is held static above the wire no reversal will occur. The reversal mechanism hinges upon the lateral motion of the tip traversing both opposite edges of the nanowire. This eliminates potential stray field writing of neighbouring wires as wires are not reversed unless they are explicitly crossed.

Crucially, the TMW process relies on the dynamic trajectory of the local tip field with no additional global external field required. This simple experimental setup has wide applicability. In strongly-interacting systems comprising dense arrays of magnetic elements (ASI for instance), the switching field of an element is significantly modified by the states of its neighbouring elements. This can lead to an increase in switching field for some elements such that writing them with a locally enhanced global field-based method will inadvertently switch other elements in the system, causing selectivity to fail. As TMW does not require globally applied fields it retains full writing functionality in strongly-interacting systems such as ASI, as shown below. This enhanced flexibility is discussed

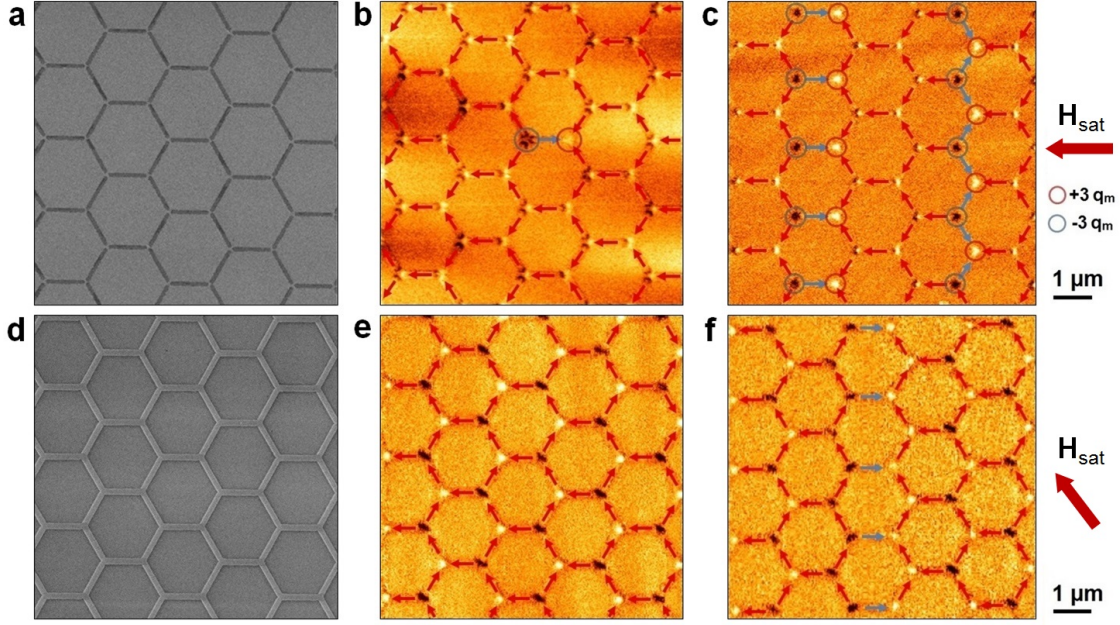


**Figure 2: Realisation of topological defect-driven magnetic writing read/write functionality in artificial spin ice.** SEM (a,d) and MFM (b,c,e,f) images demonstrating TMW written states in various ASI arrays. NiFe nanowires are  $1\ \mu\text{m}$  long,  $10\ \text{nm}$  thick. a,b,c) wires are  $75\ \text{nm}$  wide, disconnected at vertices with  $30\ \text{nm}$  gaps. d,e,f) are  $100\ \text{nm}$  wide, connected at vertices. MFM images are overlaid with arrows indicating magnetisation direction of each macrospin. Prior to imaging and writing, structures were saturated by an external field  $H_{sat}$ . Red arrows denote unwritten nanowires still magnetised along  $H_{sat}$ , blue arrows show TMW-switched wires.

b) MFM image showing a single tip-reversed nanowire, creating a pair of  $\pm 3\ q_m$  monopole-defects. c) MFM image of TMW written ‘ladder’ and zigzag ‘monopole-chain’ states. System was re-magnetised along  $H_{sat}$  between images (b) and (c).

e) MFM ‘before’ image showing all wires aligned to  $H_{sat}$ . f) MFM ‘after’ image of (e) showing a column of TMW-switched nanowires.

further in the supplementary information.

## State writing in artificial spin ice

To examine how the TMW state-writing functionality performs in an ASI system,  $1\ \mu\text{m} \times 75 \times 10\ \text{nm}^2$  nanowires were arranged into kagome ASI arrays with wires disconnected at vertices. Vertex separations of  $30\ \text{nm}$  were used, defined from the wire end to the vertex centre. Arrays were confirmed to be in a strongly-interacting ASI regime via MFM imaging of their as-grown states, with only ice-rule obeying vertices observed. Structures were initially saturated along a globally-applied field  $H_{sat}$ . TMW was then performed in zero-field to selectively reverse the magnetisation of specific macrospins until the desired microstate was reached. Figure 2 shows scanning-electron microscope (SEM) images of the ASI arrays (left-hand column) along with MFM images of initialised and TMW-written states. Figure 2 b) shows a single TMW-switched macrospin against a uniform  $H_{sat}$  aligned background, creating a pair of oppositely charged  $\pm 3\ q_m$  monopole-defect vertices without disturbing surrounding macrospins.

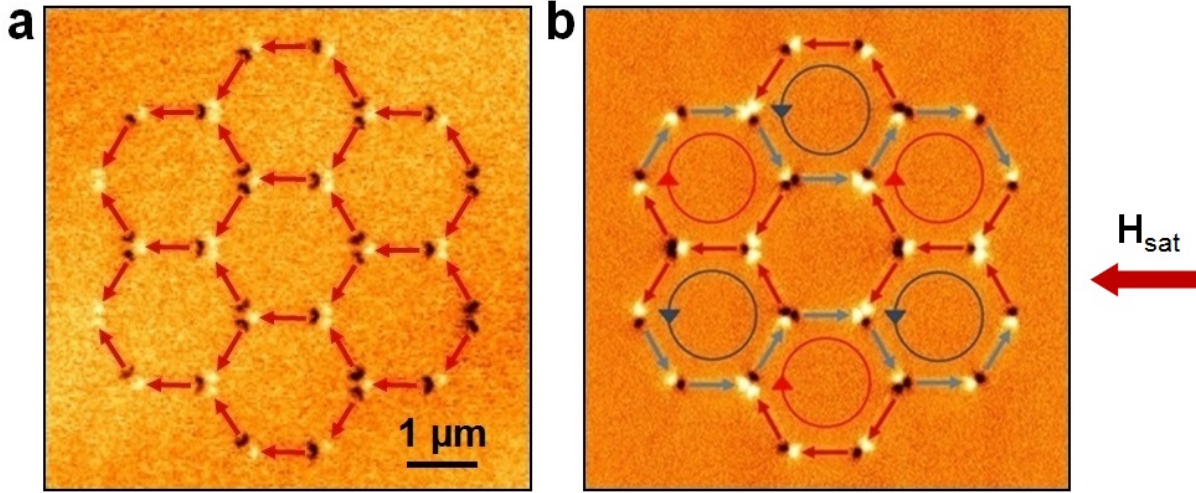


**Figure 3: Realisation of the kagome artificial spin ice ground state via topological defect-driven magnetic writing.** a) MFM image of  $1\ \mu\text{m} \times 75\ \text{nm} \times 10\ \text{nm}$  NiFe nanowires in an ASI 'rosette' with 30 nm vertex gaps. All wires are aligned to  $H_{\text{sat}}$ .

b) MFM image of the chiral spin-crystal ground state of kagome ASI, accessed via TMW writing. Reversed wires are highlighted by blue arrows. Circular arrows inside hexagons highlight the alternating-chirality magnetisation loops characterising the ground state.

This demonstrates both the spatial accuracy of TMW, allowing control of each individual macrospin, and its ability to overcome the significant energy-barriers required to create ice-rule breaking states in strongly-interacting systems, thus granting access to the full ASI manifold. Figure 2 c) shows a more complex TMW-written state containing long strings of adjacent ice-rule violating vertices, previously unobserved 'monopole-chains'. Demonstrated here are both 'ladder' (left) and zigzag (right) monopole-chains, high-energy states (due to the large number of excited  $\pm 3\ q_m$  vertices) with low entropy (due to the relatively few ways to arrange such configurations on an ASI array). This combination of high energy with low entropy results in a state exceedingly difficult to realise via conventional means and also fulfills the criteria for exhibiting 'negative temperature' - predicted to exist in ASI<sup>29</sup> and discussed further below. Such states highlight the novel and unexplored regions of the ASI manifold now accessible using TMW. Even in these high-energy states the system retains its written configuration with high stability, undisturbed by the MFM imaging process and maintaining microstate fidelity over several months.

So far, only disconnected nanowires have been considered. To test the flexibility of TMW in varied architectures, ASI arrays were fabricated with nanowires connected at vertices. Figure 2 d) is an SEM image of  $1\ \mu\text{m} \times 150 \times 10\ \text{nm}^2$  nanowires in a connected kagome ASI array. Figure 2 e) shows MFM imaging of the same array with macrospins saturated along  $H_{\text{sat}}$ . TMW was then used to reverse a central column of macrospins, with fig. 2 f) showing the successfully-written resultant state. The TMW writing process is seen to retain its functionality in systems comprising connected nanowires, opening up microstate writing in a huge range of potential systems.

## Realisation of the kagome artificial spin ice ground state

One ASI microstate which has received significant attention while eluding observation is the spin-crystal ground state of dipolar kagome ASI. The ground state of the frustrated kagome lattice has been of interest in both natural and artificial systems, with the ground state of natural systems consisting of point-spins only recently reported after years of investigation<sup>35</sup>. Point-spin systems interact via nearest-neighbour exchange interactions, hence the difficulty in identifying a long-range ordered ground state. However, when considering dipoles of finite length (i.e. artificial macrospins), further neighbour interactions (multipolar terms) break the degeneracy of ice-rule states as long-range magnetic charge and spin order are imposed<sup>36-38</sup>. This leads to a well-defined ground state in ASI, existing when both charge and spin order are present throughout the entire system. A quasi-ground state in a partial ‘building block’ kagome ASI system comprising just 1-3 hexagons has been demonstrated<sup>39</sup>, but the smallest system supporting a true ground state unit-cell which can tile infinitely over the kagome lattice is the 30 macrospin ‘rosette’ shown in figure 3. Attempts have been made to thermally activate then anneal into the ground state on a rosette-sized system<sup>18</sup>, but the near-degenerate energies of all ice-rule obeying microstates and the low entropy of the ground state (2 configurations in  $2^{30}$ ) have rendered efforts ineffectual. A simple and convenient means to reliably access the spin-crystal ground state will allow closer examination of the divergence between true and artificial ice-like systems, a major point of interest in the field. As such, demonstrating the first experimental realisation of the spin-crystal kagome ground state is a perfect opportunity for testing the capabilities of TMW.

Figure 3 a) shows an MFM image of a kagome ASI rosette comprising  $1\ \mu\text{m} \times 75 \times 10\ \text{nm}^2$  nanowires with all macrospins aligned along  $H_{sat}$ . TMW was then performed in zero-field to selectively remagnetise 14 of the 30 macrospins, with the resultant state shown in fig. 3 b). The macrospins in each of the outer hexagons now lie in closed continuous spin-loops, with chirality alternating between adjacent hexagons (highlighted by circular arrows within hexagons). This configuration not only satisfies the ice-rules but also exhibits magnetic charge and spin order, with the observed charge and spin configurations exactly matching those previously reported in theoretical schematics of the spin-crystal ground state<sup>18,30,36,37,40</sup>. As such, we conclude that the TMW-written state presented here represents an experimentally-realised kagome ground state. That states eluding observation up to this point, despite direct efforts to prepare them, may now be written to order using readily-available equipment is an important threshold development for the fields of ASI and scanning probe patterning. A TMW-realised alternate-chirality ground state is presented in figure S3 of the supplementary information.

## Negative effective temperature states in artificial spin ice

As well as providing reliable access to low-energy states, TMW also significantly expands the accessible ASI microstate space by allowing preparation of high-energy, low-entropy microstates such as the monopole-chains discussed above. In general, the thermal anneals used to prepare ASI states work by keeping ASI systems in thermodynamic equilibrium with an (effective, in the case of field protocols) heat bath. As the temperature of the heat bath is reduced, the ASI settles into a low-energy state with relatively few ice-rule defects. Rotating-field protocols may be thought of in a similar way by assigning them an effective temperature based on the field step-size and treating

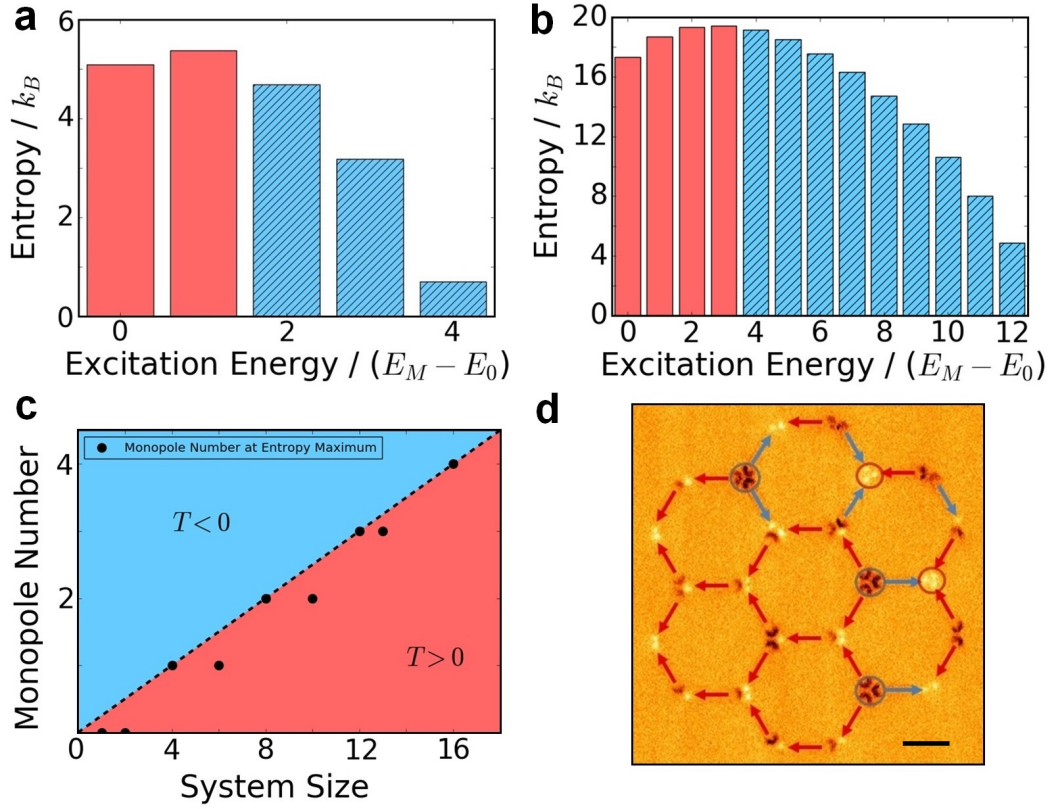


**Figure 4: Negative effective temperature in artificial spin ice.**

Entropy vs. excitation energy histograms for **a**) a four-vertex and **b**) a twelve-vertex kagome ASI system. Excitation energy normalised by  $E_M - E_0$  corresponds to number of monopole vertices present. Red bars denote positive temperature states, shaded blue bars indicate negative effective temperatures.

**c**) Effective temperature phase diagram for one-to-eighteen vertex kagome ASI systems. Negative effective temperatures arise when more than one-quarter of total vertices are in monopole-defect configuration.

**d**) MFM image of a twelve-vertex (counting three-macrospin vertices only) kagome ASI rosette. Five monopole-defect vertices are observed, indicating a negative effective temperature state. Scale bar indicates 1  $\mu\text{m}$ .

them as a heat bath<sup>29</sup>. In contrast to these methods, TMW can reliably prepare ASI in states that are inherently out-of-equilibrium. For example, it is vanishingly improbable that a microstate with 19 monopoles on a system of 40 honeycomb vertices as shown in figure 2 c) would occur through any sort of equilibration process with a heat bath of finite temperature. To formalise this idea, it is useful to invoke the concept of an effective spin temperature for ASI as introduced by Nisoli *et al*<sup>29</sup>. In statistical mechanics, the temperature of a system is formally defined as a measure of how the energy of that system varies with disorder  $T = \frac{\partial U}{\partial S}$ . Taking into account only nearest-neighbour interactions (which dominate ASI energetics), the energy of an ASI system is determined by the number of monopoles (ice-rule violations) in the system, with each monopole raising the total energy by the difference in energy between a monopole and ice-rule vertex,  $\Delta E = E_M - E_0$ . The total energy of the system is thus given by  $E = E_{ice} + n\Delta E$ , where  $E_{ice}$  is the system energy when all vertices obey ice-rules and  $n$  is the number of monopoles. Since the fully ice-rule compliant state is highly degenerate but the fully excited state (where every vertex hosts a monopole) has just two possible configurations (spin-degeneracy), there must exist a range of microstates with negative effective temperatures<sup>41,42</sup>. Such states are precisely those difficult to access via thermal and rotating field protocols, but trivial to realise via TMW. It is worth briefly stating that assigning a state an effective temperature does not necessarily imply that state is thermally active, the activation energy of the systems considered here is  $\sim 10^5$  K. Effective temperatures instead describe the local shape of the energy and entropy landscape<sup>43-45</sup>.

By directly enumerating the number of monopoles (and therefore system energy) for all microstates in small kagome ASI systems and plotting monopole number versus entropy (figure 4 a-c), the sign of the effective temperature may be clearly visualised from the gradient  $\frac{\partial U}{\partial S}$ . Figures 4 a) and b) show this relation between entropy and energy/monopole-number in four and twelve-vertex systems respectively, with a clear change in gradient and associated transition to negative temperature occurring in both when over a quarter of vertices host monopole defects. The effective temperatures of all microstates in 1-18 vertex systems were calculated, with results shown as a phase diagram in fig. 4 c). For all system-sizes negative temperatures were seen to correspond to microstates in which over a quarter of total vertices were monopole-defects. The five-monopole microstate on a 12-vertex honeycomb rosette shown in figure 4 d) thus corresponds to a negative temperature state directly written by TMW, as does the monopole-chain state shown in fig. 2 c). By comparison, the rosette system in fig. 4 d) would have to be heated to almost  $10^5$  K and cooled near-instantaneously to have a 0.1% chance of leaving the system in a five-monopole state. ASI enables direct room-temperature access to the complex and exotic physics of frustrated magnetism, with system energetics and time-scales easily tunable via fabrication. Adding to prior observations of otherwise-elusive ice-rule behaviour<sup>6</sup> and monopole-defects<sup>3</sup>, TMW now introduces ASI as a model-system in which to study the dynamics and evolution of negative temperature states.

## Conclusions

In this article we have presented an outline and demonstration of topological defect-driven magnetic writing, a powerful and simple-to-use writing technique broadening the field of magnetic scanning probe patterning and allowing unprecedented access to novel and exotic states in artificial spin ice and related nanomagnetic systems. Reconfigurable magnetic metamaterials and the associated technological benefits are now a realistic and practical

prospect, setting the scene for a period of rapid development as long-proposed designs including hardware neural-networks and reconfigurable magnonic crystals may now be experimentally realised. The spin-crystal ground state and negative-temperature monopole-chain states written in this work are evidence that all possible magnetic configurations are now accessible, both previously studied yet hard-to-access states through to states exhibiting exciting new physics, considered unattainable until now.

While the ultimate throughput of any scanning probe technique is limited by the mechanical nature of a moving tip, the magnetic charge supplied here by an magnetic force microscope tip may come from a number of sources. A domain wall in a nanowire of the dimensions discussed here has  $q_m \approx 10^{-9}$  Am, within the limits for achieving topological defect-driven magnetic writing. One can envisage a system comprising a three-dimensional network of nanowires whereby current-controlled domain walls replace the magnetic force microscope tip, greatly enhancing flexibility, throughput and integration with existing technologies.

## Methods

### Structures and fabrication

Nanostructures were fabricated using an electron beam lithography lift-off process with PMMA resist. Permalloy (nominally  $\text{Ni}_{81}\text{Fe}_{19}$ ) of 10 nm thickness was deposited by thermal evaporation onto Si/SiO<sub>2</sub> substrates.

### Magnetic force microscopy

The magnetic charge states of nanostructures were written and measured using MFM with HM and LM tips respectively. MFM is directly sensitive to magnetic charge<sup>46</sup>, providing an ideal tool to read and write magnetic charge landscapes. Two MFM systems were used, a Dimension 3100 and an Asylum MFP-3D. An interface was developed to define the path of the tip relative to the nanopatterned structures (and therefore the magnetic state to be written) graphically, by drawing over an existing AFM/MFM image or CAD schematic, or by defining an  $(x, y)$  position list. Writing does not occur when the tip-sample separation is over 5-10 nm, allowing for free movement of the tip around samples between writing events by raising the tip. Writing operations were performed with the tip moving perpendicular to the wire length. MFM imaging was performed in a tapping mode at lift-heights of 35-45 nm. The HM and LM tips have moments and stray fields of  $\sim 5 \times 10^{-13}$  emu, 690 Oe and  $\sim 3 \times 10^{-14}$  emu, 320 Oe respectively<sup>47</sup>, with stray fields measured at a typical AFM tip-sample separation ( $\sim 2$ -5 nm) from the tip apex. Experimental determination of the monopole-like magnetic charge associated with MFM tips is challenging, but prior work using Lorentz electron tomography have arrived at values of  $\sim 10^{-8}$  Am<sup>48</sup>, similar to those simulated here. Writing has been successfully performed on wire-like structures of widths and lengths up to 150 nm and 4  $\mu\text{m}$  with tip speeds of up to 400  $\mu\text{m/s}$ . Significantly faster tip speeds of up to 200 m/s show successful writing in micromagnetic simulations but cannot yet be experimentally tested using our current equipment.

## Micromagnetic simulation

Additional insight into the reversal dynamics of the nanowires was provided by performing a series of micromagnetic simulations using the object-oriented micromagnetic framework (OOMMF)<sup>49</sup>. Typical micromagnetic parameters for permalloy were used, i.e. saturation magnetisation,  $M_S = 860 \times 10^3$  A/m, exchange stiffness,  $A = 13 \times 10^{-12}$  J/m, zero magnetocrystalline anisotropy and a Gilbert damping parameter,  $\alpha = 0.01$ . The point probe approximation (that at small tip-sample separations an MFM tip may be described by a point monopole moment<sup>31,32</sup>) was used. This approximation is widely used in MFM simulations and previous work analysing systems with similar dynamics has shown that both dipolar and monopolar-modelled tip fields induce tip-localised magnetisation vortices in ferromagnetic thin films<sup>33,34</sup>.

The simulated nanowires were 10 nm thick with widths of 75 nm and were divided into  $2.5 \times 2.5 \times 10$  nm cells. Finite-length wires of 0.5-3  $\mu\text{m}$  length were studied along with a semi-infinite wire of 10  $\mu\text{m}$  length where the demagnetisation effects from the wire ends were corrected for by the inclusion of plates of fixed magnetic charge at the nanowire ends<sup>50</sup>.

The field from the MFM tip was modelled as a single magnetic charge,  $q_{tip}$ , producing a radial field  $H = \frac{\mu_0}{4\pi} \frac{q_{tip}}{r^2}$  at a distance  $r$  from the charge. During the simulation this magnetic charge moved perpendicular to the nanowire axis in 1 nm steps every 10 ps representing a velocity of 100 m/s. This is faster than the velocities of  $\sim 10^{-4}$  m/s investigated experimentally. However, the simulated speed is well below those associated with exciting any precessional spin modes and is believed to be reasonable in this case. To avoid a discrete jump in applied field on the nanowire when starting the simulation, the magnetic charge was initialised 300 nm away from the nanowire in the plane of the wire. Following the magnetic charge interaction with the wire, the wire was allowed to relax to an energetically stable state in zero field to obtain its final configuration.

## Additional information

Supplementary information is available in the online version of the paper. Reprints and permission information is available online at [www.nature.com/reprints](http://www.nature.com/reprints). Correspondence and requests for materials should be addressed to JCG.

## Author contributions

JCG with the assistance of DMA, DMB and WRB conceived the experiment, JCG fabricated the samples and performed the experimental measurements, JCG, VB and AM developed the practical selective writing capabilities on SPM systems, JCG, DMA and DMB performed micromagnetic simulations, JCG performed the experimental measurements, DMA performed the effective temperature analysis. JCG, DMA, WRB and LFC contributed to the manuscript. All authors contributed to discussions informing the research.

## Acknowledgements

This work was supported by the Engineering and Physical Sciences Research Council [grant number EP/G004765/1] and the Leverhulme Trust [grant number RPG 2012-692] to WRB and supported by the Engineering and Physical Sciences Research Council [grant number EP/J014699/1] to LFC.

## Data availability statement

Data requests should be addressed to dataenquiryexss@imperial.ac.uk.

## Competing interests

The authors declare no competing financial interests.

## References

1. Pauling, L. The structure and entropy of ice and of other crystals with some randomness of atomic arrangement. *Journal of the American Chemical Society* **57**, 2680–2684 (1935).
2. Wang, R. F. *et al.* Artificial 'spin ice' in a geometrically frustrated lattice of nanoscale ferromagnetic islands. *Nature* **439**, 303–6 (2006).
3. Ladak, S., Read, D., Perkins, G. K., Cohen, L. F. & Branford, W. Direct observation of magnetic monopole defects in an artificial spin-ice system. *Nat. Phys.* **6**, 359–363 (2010).
4. Mengotti, E. *et al.* Real-space observation of emergent magnetic monopoles and associated Dirac strings in artificial kagome spin ice. *Nat. Phys.* **7**, 68–74 (2010).
5. Nisoli, C. *et al.* Ground State Lost but Degeneracy Found: The Effective Thermodynamics of Artificial Spin Ice. *Phys. Rev. Lett.* **98**, 217203 (2007).
6. Qi, Y., Brintlinger, T. & Cumings, J. Direct observation of the ice rule in an artificial kagome spin ice. *Phys. Rev. B* **77**, 094418 (2008).
7. Morgan, J. P., Stein, A., Langridge, S. & Marrows, C. H. Thermal ground-state ordering and elementary excitations in artificial magnetic square ice. *Nat. Phys.* **7**, 75–79 (2010).
8. Lammert, P. E. *et al.* Direct entropy determination and application to artificial spin ice. *Nat. Phys.* **6**, 786–789 (2010).
9. Branford, W., Ladak, S., Read, D., Zeissler, K. & Cohen, L. F. Emerging chirality in artificial spin ice. *Science* **335**, 1597–600 (2012).

10. Farhan, a. *et al.* Direct Observation of Thermal Relaxation in Artificial Spin Ice. *Phys. Rev. Lett.* **111**, 057204 (2013).
11. Budrikis, Z., Politi, P. & Stamps, R. L. A network model for field and quenched disorder effects in artificial spin ice. *New Journal of Physics* **14**, 045008 (2012).
12. Heyderman, L. J. & Stamps, R. Artificial ferroic systems: novel functionality from structure, interactions and dynamics. *J. Phys. Condens. Matt.* **25**, 363201 (2013).
13. Ladak, S., Read, D., Tyliczszak, T., Branford, W. & Cohen, L. F. Monopole defects and magnetic Coulomb blockade. *New J. Phys.* **13**, 023023 (2011).
14. Grundler, D. Reconfigurable magnonics heats up. *Nature Physics* **11**, 438–441 (2015).
15. Krawczyk, M. & Grundler, D. Review and prospects of magnonic crystals and devices with reprogrammable band structure. *Journal of Physics: Condensed Matter* **26**, 123202 (2014).
16. Zhang, S. *et al.* Crystallites of magnetic charges in artificial spin ice. *Nature* **500**, 553 (2013).
17. Farhan, A. *et al.* Exploring hyper-cubic energy landscapes in thermally active finite artificial spin-ice systems. *Nature Physics* **9**, 375–382 (2013).
18. Farhan, A. *et al.* Thermally induced magnetic relaxation in building blocks of artificial kagome spin ice. *Physical Review B* **89**, 214405 (2014).
19. Kapaklis, V. *et al.* Thermal fluctuations in artificial spin ice. *Nature nanotechnology* **9**, 514–519 (2014).
20. Garcia, R., Knoll, A. W. & Riedo, E. Advanced scanning probe lithography. *Nature nanotechnology* **9**, 577–587 (2014).
21. Eigler, D. M. & Schweizer, E. K. Positioning single atoms with a scanning tunnelling microscope. *Nature* **344**, 524–526 (1990).
22. Van Loenen, E., Dijkamp, D., Hoeven, A., Lenssinck, J. & Dieleman, J. Direct writing in si with a scanning tunneling microscope. *Applied Physics Letters* **55**, 1312–1314 (1989).
23. Pavliček, N. *et al.* Synthesis and characterization of triangulene. *Nature Nanotechnology* (2017).
24. Albisetti, E. *et al.* Nanopatterning reconfigurable magnetic landscapes via thermally assisted scanning probe lithography. *Nature nanotechnology* (2016).
25. Krause, S., Berbil-Bautista, L., Herzog, G., Bode, M. & Wiesendanger, R. Current-induced magnetization switching with a spin-polarized scanning tunneling microscope. *Science* **317**, 1537–1540 (2007).
26. Gartside, J., Burn, D., Cohen, L. & Branford, W. A novel method for the injection and manipulation of magnetic charge states in nanostructures. *Scientific Reports* **6** (2016).
27. Wang, Y.-L. *et al.* Rewritable artificial magnetic charge ice. *Science* **352**, 962–966 (2016).

28. Mermin, N. D. The topological theory of defects in ordered media. *Rev. Mod. Phys.* **51**, 591–648 (1979).
29. Nisoli, C. *et al.* Effective temperature in an interacting vertex system: theory and experiment on artificial spin ice. *Physical review letters* **105**, 047205 (2010).
30. Anghinolfi, L. *et al.* Thermodynamic phase transitions in a frustrated magnetic metamaterial. *Nature communications* **6** (2015).
31. Hartmann, U. The point dipole approximation in magnetic force microscopy. *Phys. Lett. A* **137**, 475–478 (1989).
32. Lohau, J., Kirsch, S., Carl, A., Dumpich, G. & Wassermann, E. F. Quantitative determination of effective dipole and monopole moments of magnetic force microscopy tips. *J. Appl. Phys.* **86**, 3410 (1999).
33. Magiera, M. P., Hucht, A., Hinrichsen, H., Dahmen, S. R. & Wolf, D. E. Magnetic vortices induced by a moving tip. *EPL (Europhysics Letters)* **100**, 27004 (2012).
34. Magiera, M. P. & Schulz, S. Magnetic vortices induced by a monopole tip. *Magnetics, IEEE Transactions on* **50**, 1–4 (2014).
35. Liao, H. *et al.* Gapless spin-liquid ground state in the  $s = 1/2$  kagome antiferromagnet. *Physical Review Letters* **118**, 137202 (2017).
36. Möller, G. & Moessner, R. Magnetic multipole analysis of kagome and artificial spin-ice dipolar arrays. *Physical Review B* **80**, 140409 (2009).
37. Chern, G.-W., Mellado, P. & Tchernyshyov, O. Two-stage ordering of spins in dipolar spin ice on the kagome lattice. *Physical review letters* **106**, 207202 (2011).
38. Rougemaille, N. *et al.* Artificial kagome arrays of nanomagnets: a frozen dipolar spin ice. *Physical Review Letters* **106**, 057209 (2011).
39. Arnalds, U. B. *et al.* Thermalized ground state of artificial kagome spin ice building blocks. *Applied Physics Letters* **101**, 112404 (2012).
40. Chern, G.-W. & Tchernyshyov, O. Magnetic charge and ordering in kagome spin ice. *Philosophical Transactions of the Royal Society of London A: Mathematical, Physical and Engineering Sciences* **370**, 5718–5737 (2012).
41. Purcell, E. M. & Pound, R. V. A nuclear spin system at negative temperature. *Physical Review* **81**, 279 (1951).
42. Abraham, E. & Penrose, O. Physics of negative absolute temperatures. *Physical Review E* **95**, 012125 (2017).
43. Cugliandolo, L. F. The effective temperature. *Journal of Physics A: Mathematical and Theoretical* **44**, 483001 (2011).
44. Fierro, A., Nicodemi, M. & Coniglio, A. Thermodynamics and statistical mechanics of frozen systems in inherent states. *Physical Review E* **66**, 061301 (2002).

45. Martiniani, S., Schrenk, K. J., Ramola, K., Chakraborty, B. & Frenkel, D. Numerical test of the edwards conjecture shows that all packings are equally probable at jamming. *Nature Physics* (2017).
46. Hubert, A., Rave, W. & Tomlinson, S. L. Imaging magnetic charges with magnetic force microscopy. *physica status solidi (b)* **204**, 817–828 (1997).
47. Jaafar, M., Asenjo, A. & Vazquez, M. Calibration of coercive and stray fields of commercial magnetic force microscope probes. *IEEE transactions on nanotechnology* **7**, 245–250 (2008).
48. McVitie, S., Ferrier, R., Scott, J., White, G. & Gallagher, A. Quantitative field measurements from magnetic force microscope tips and comparison with point and extended charge models. *Journal of Applied Physics* **89**, 3656–3661 (2001).
49. Donahue, M. & Porter, D. Oommf (1999).
50. McMichael, R. & Donahue, M. Head to head domain wall structures in thin magnetic strips. *IEEE Trans. Magn.* **33**, 4167 (1997).